Earth and Planetary Science Letters 515 (2019) 248–259

Contents lists available at ScienceDirect

Earth and Planetary Science Letters

www.elsevier.com/locate/epsl

Hydrothermal circulation cools continental crust under exhumation

Wenrong Cao [a,*], Cin-Ty A. Lee [b], Jiaming Yang [a], Andrew V. Zuza [c]

[a] Department of Geological Sciences and Engineering, University of Nevada, Reno, MS-172, 1664 N. Virginia St., Reno, NV 89557, United States of America
[b] Department of Earth, Environmental and Planetary Sciences, Rice University, MS-126, 6100 Main Street, Houston, TX 77005, United States of America
[c] Nevada Bureau of Mines and Geology, University of Nevada, Reno, MS-178, 1664 N. Virginia St., Reno, NV 89557, United States of America

ARTICLE INFO

Article history:
Received 5 October 2018
Received in revised form 17 February 2019
Accepted 18 March 2019
Available online xxxx
Editor: R. Bendick

Keywords:
hydrothermal circulation
continental crust
erosion
Nusselt number
surface heat flux
crustal rheology

ABSTRACT

The formation of continental crust in magmatic arcs involves cooling of hot magmas to a relatively colder crust enhanced by exhumation and hydrothermal circulation in the upper crust. To quantify the influence of these processes on the thermal and rheological states of the crust, we developed a one-dimensional thermal evolution model, which invokes conductive cooling, advection of crust by erosion-driven exhumation, and cooling by hydrothermal circulation. We parameterized hydrothermal cooling by adopting depth-dependent effective thermal conductivity, which is determined by the crustal permeability structure and the prescribed Nusselt number at the surface. Different combinations of erosion rate and Nusselt number were tested to study the evolution of crustal geotherms, surface heat flux, and cooling rate. Simulations and scaling analyses quantify how erosion and hydrothermal circulation promote cooling via increasing total surface heat flux compared to pure conductive cooling. Hydrothermal circulation imposes intense short-term and persistent long-term cooling effects. Thinner, warmer, fast exhuming crust, with higher permeability and more vigorous hydrothermal circulation, leads to higher steady-state total surface heat flux. Hydrothermal cooling at steady state is more effective when the Péclet number is small. Hydrothermal cooling also changes crustal rheological state and thickens the brittle crust. This in turn promotes the initiation of brittle deformation in the upper crust in magmatic arcs or in regions undergoing exhumation. Interpretation of low-temperature thermochronological data could overestimate average cooling rates if hydrothermal cooling is not considered.

1. Introduction

The formation of continental crust in magmatic orogens (i.e., continental arcs) is characterized by distinct evolution of the composition, structure, and thermal state of the crust. In a magmatic orogen, the arc cools from magmatic temperatures (700-1200 °C) to relatively cold temperatures (<400 °C) on timescales of tens of millions of years. Although much of this cooling is controlled by conduction, both exhumation and hydrothermal cooling may also play a role. For example, most magmatic orogens are accompanied by crustal thickening and subsequent isostatic elevation increase, which drives erosion (Allmendinger et al., 1997; Lee et al., 2015; Cao and Paterson, 2016; Jiang and Lee, 2017) that cools the exhuming deeper, hotter rocks.

High elevations and topographic gradient also drive meteoric precipitation, which provides a steady supply of water to drive hydrothermal circulation in the uppermost crust.

Cooling of a magmatic orogen thus involves conduction, advection of crust due to erosion-driven exhumation, and hydrothermal cooling (Fig. 1). Conductive and advective cooling have been widely discussed in the field of thermochronology to estimate cooling and exhumation rates (e.g., Stüwe et al., 1994; Reiners and Brandon, 2006; Braun et al., 2012). Hydrothermal circulation has been well studied at mid-ocean ridges where circulation of seawater promotes the cooling of oceanic lithosphere (e.g., Morgan and Chen, 1993; Roland et al., 2010). However, despite the well-known fact that hydrothermal circulation plays a crucial role in regional metamorphism and ore-formation (e.g., Manning and Ingebritsen, 1999; Fekete et al., 2016), regional cooling effects associated with hydrothermal processes in continental settings have received less attention (Ingebritsen et al., 1989; Manga, 1998; Kooi, 2016; Diamond et al., 2018). While many studies have focused on individual intrusion-wallrock systems (e.g., Cathles, 1977; Hayba and Ingebritsen, 1997), few studies have simultaneously incorporated conduction, erosion, and hydrothermal circulation to evaluate their relative importance in cooling continental crust and how these processes together affect the total surface heat flux, crustal thermal state, and crustal rheology. Understanding these

* Corresponding author.
E-mail address: wenrongc@unr.edu (W. Cao).

https://doi.org/10.1016/j.epsl.2019.03.029
0012-821X/

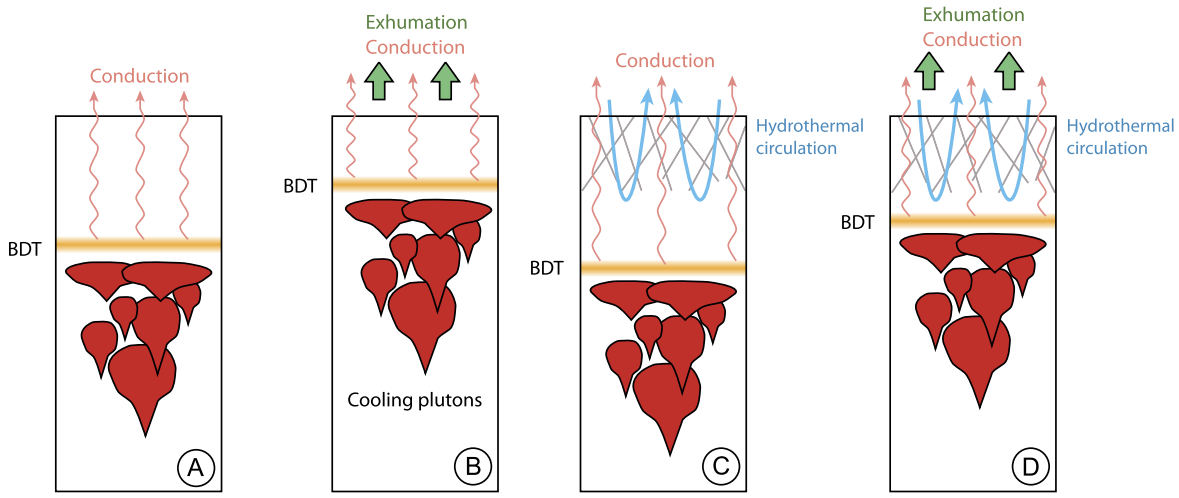

Fig. 1. Conceptional models of cooling a continental arc crust via (A) conduction only; (B) combination of conduction and erosion-driven exhumation; (C) combination of conduction and hydrothermal circulation; (D) combination of conduction, exhumation, and hydrothermal circulation. BDT: Brittle-Ductile Transition. (For interpretation of the colors in the figure(s), the reader is referred to the web version of this article.)

cooling processes collectively is important because the thermal evolution of the crust influences the strength, brittle-ductile transition depth, and the initiation, localization, and geometry of brittle faults (e.g., Sibson, 1982; Zuza et al., 2017; Zuza and Carlson, 2018).

In this study, we use a one-dimensional (1-D) numerical model and scaling analyses to investigate the thermal evolution of a continental arc crust subjected to simultaneous surface erosion and hydrothermal circulation. We address the following questions: What are the contributions of conductive, erosion, and hydrothermal circulation to the thermal evolution of the crust? How do thermal and rheological profiles, surface heat flux, and crustal cooling rate evolve? Finally, we discuss some potential geologic examples in the Cretaceous Sierra Nevada arc and implications of hydrothermal circulation for promoting regional cooling and the initiation of brittle deformation in the upper crust.

2. Conductive cooling and effect of erosion

Before introducing the hydrothermal circulation into a numerical model, we begin with a brief review of the governing equations and scaling relationships for conductive cooling and the effect of erosion-driven exhumation. One-dimensional thermal evolution of a lithospheric column during conduction and erosion is governed by:

$$\rho C_p \left(\frac{\partial T}{\partial t} - \frac{dT}{dz} \cdot E \right) = \lambda_0 \frac{\partial^2 T}{\partial z^2} \tag{1}$$

where T is the temperature at depth z, t is time, ρ is the density of the crust, C_p is the heat capacity of rock, λ_0 is the normal thermal conductivity of rock, and E is surface erosion or exhumation rate (see Table S1 for descriptions of variables and constants). Radiogenic heat production is omitted for simplicity because the timescales investigated here are short ($\sim 10^1$ Myr).

Erosion-driven exhumation advects deeper and warmer crust towards the surface and thus increases the geothermal gradient. The strength of erosional advection relative to thermal conduction is given by the Péclet number (Pe), the ratio between the time scale of conduction (L^2/κ_0) and advection (L/E):

$$Pe = \frac{EL}{\kappa_0} \tag{2}$$

where L is the thickness of the crust or lithosphere, which can vary from 1 to 100 km depending on the subject of interest, and κ_0 is the normal thermal diffusivity of rock ($\kappa_0 = \lambda_0/(\rho Cp)$). If $Pe = 0$, there is no advection. If $Pe = 1$, advection is of equal strength as conduction. The steady-state geothermal profile during conduction and advection is given by (Stüwe et al., 1994; Batt and Brandon, 2002):

$$T(z) = T_s + (T_L - T_s) \cdot \frac{1 - \exp(-Pe \cdot \frac{z}{L})}{1 - \exp(-Pe)} \tag{3}$$

where T_s and T_L are temperatures at the surface and the bottom of crustal-lithospheric column, respectively. At steady state, the surface heat flux of conduction and erosional advection (q_{CE}) has the following relationship with the steady-state conductive surface heat flux (q_C) (Stüwe et al., 1994; Batt and Brandon, 2002):

$$q_{CE} = q_C \cdot \frac{Pe}{1 - \exp(-Pe)} \tag{4}$$

The characteristic time of the conduction-erosion case can be derived by nondimensionalizing Eq. (1):

$$\tau_{CE} = \frac{L^2}{\kappa_0 (1 + Pe)} \tag{5}$$

If $Pe \to 0$, Equations (3)–(5) describe the steady-state geothermal profile, surface heat flux (q_C), and characteristic time (τ_C) of the purely conductive case. If $Pe > 0$, we have $q_{CE} > q_C$, which suggests that advection enhances the surface heat flux. Table 1 compares the different cooling processes.

3. Numerical model invoking hydrothermal circulation

3.1. Introducing hydrothermal circulation into governing equation

In the upper crust, if the crustal permeability (k_φ) is larger than a critical value (typically 10^{-16}–10^{-17} m^2) (Manning and Ingebritsen, 1999) and assuming that the rocks are fluid-saturated, heat transport by hydrothermal circulation can be important. In magmatic orogens, both topography-driven flow and density-driven flow could occur. The former is caused by the difference of hydraulic heads associated with topographic gradient while the latter is thermal convection of fluids driven by deeper magmatic heat sources. Topography-driven flow dominates in upper crust while density-driven flow becomes more important in the deeper upper-middle crust where topographic drive diminishes (e.g., Ingebritsen et al., 1989).

Table 1
Comparison of different cooling processes.

	Governing equation	Char. length	Char. time	Steady-state geothermal profile	Steady-state surface heat flux	Note
Conduction	$\rho C_p \frac{\partial T}{\partial t} = \lambda_0 \frac{\partial^2 T}{\partial z^2}$	$\sqrt{\kappa_0 t}$	$\frac{L^2}{\kappa_0}$	$T_s + \Gamma \cdot z$	$\lambda_0 \cdot \Gamma$	$\Gamma = \frac{T_L - T_s}{L}$, $\kappa_0 = \frac{\lambda_0}{\rho C_p}$
Conduction + erosion	$\rho C_p (\frac{\partial T}{\partial t} - \frac{dT}{dz} \cdot E) = \lambda_0 \frac{\partial^2 T}{\partial z^2}$	$\sqrt{\kappa_0 t(1+Pe)}$	$\frac{L^2}{\kappa_0(1+Pe)}$	$T_s + \Gamma \cdot L \cdot \frac{1-\exp(-\frac{Ez}{\kappa_0})}{1-\exp(-Pe)}$	$\lambda_0 \cdot \Gamma \cdot \frac{Pe}{1-\exp(-Pe)}$	$Pe = \frac{EL}{\kappa_0}$
Conduction + hydrothermal circulation	$\rho C_p \frac{\partial T}{\partial t} = \frac{\partial}{\partial z} \lambda_{eq}(z) \frac{\partial T}{\partial z}$	$\sqrt{\overline{\kappa} t}$	$\frac{L^2}{\overline{\kappa}}$	$T_s + \int_0^z \frac{\overline{\lambda} \cdot \Gamma \cdot dz}{\lambda_{eq}(z)}$	$\lambda_0 \cdot \Gamma \cdot \gamma$	$\overline{\lambda} = \{\frac{1}{L} \int_0^L \frac{dz}{\lambda_{eq}(z)}\}^{-1}$ $\overline{\kappa} = \frac{\overline{\lambda}}{\rho C_p}$, $\gamma = \frac{\overline{\lambda}}{\lambda_0}$
Conduction + erosion + hydrothermal circulation	$\rho C_p (\frac{\partial T}{\partial t} - \frac{dT}{dz} \cdot E) = \frac{\partial}{\partial z} \lambda_{eq}(z) \frac{\partial T}{\partial z}$	$\sqrt{\overline{\kappa} t(1+Pe')}$	$\frac{L^2}{\overline{\kappa}(1+Pe')}$	$T_s + \int_0^z \frac{\overline{\lambda} \cdot \Gamma}{\lambda_{eq}(z)} \cdot \frac{Pe' \cdot dz}{1-\exp(-Pe')}$	$\lambda_0 \cdot \Gamma \cdot \frac{Pe'}{1-\exp(-Pe')} \cdot \gamma$	$Pe' = \frac{EL}{\overline{\kappa}}$

T: Temperature. z: Depth. t: Time. ρ: Density of rocks. C_p: Specific heat capacity of rock. λ_0: Normal thermal conductivity of rock. κ_0: Normal thermal diffusivity of rock. L: Thickness of crust or lithosphere. T_S: Surface temperature. T_L: Temperature at bottom of crustal-lithospheric column. Γ: Liner geothermal gradient. E: Erosion rate. Pe: Péclet number of surface erosion. Pe': Modified Péclet number. $\overline{\lambda}$: Bulk average thermal conductivity. $\overline{\kappa}$: Bulk average thermal diffusivity. $\lambda_{eq}(z)$: Depth-dependent effective thermal conductivity. γ: Ratio of bulk average thermal conductivity to normal thermal conductivity. Char. length/time: Characteristic length/time.

Many simulation studies have employed fluid-rock systems to explore hydrothermal circulation (e.g., Travis et al., 1991; Ingebritsen et al., 2010). Alternatively, studies focusing on the thermal effect of hydrothermal circulation adopt an effective thermal conductivity (λ_{eq}) to account for the additional heat transfer via hydrothermal circulation (e.g., Morgan, 1987; Roland et al., 2010). Most studies of the latter type have linked λ_{eq} with the Nusselt number (Nu), a dimensionless number which compares the relative importance of the total heat flux (q_T) versus conductive heat flux (q_C) (e.g., Morgan, 1987; Roland et al., 2010; Schmeling and Marquart, 2014), that is:

$$Nu = \frac{q_T}{q_C} \tag{6}$$

The total heat flux here is the sum of hydrothermal heat flux (q_H) and the conductive heat flux (q_C). If there is no hydrothermal heat transport, $q_H = 0$, and $Nu = 1$. When $Nu > 1$, the total heat flux is modulated by additional heat transport. In this study, we have prescribed a depth-dependent Nu to derive λ_{eq}, similar to the implementation in Roland et al. (2010). The effective thermal conductivity is defined as:

$$\lambda_{eq} = \lambda_0 \cdot Nu \tag{7}$$

The governing equation (Eq. (1)) can be rewritten by taking both conduction and hydrothermal circulation into account:

$$\rho C_p \left(\frac{\partial T}{\partial t} - \frac{dT}{dz} \cdot E \right) = \frac{\partial}{\partial z} \lambda_{eq} \frac{\partial T}{\partial z} \tag{8}$$

Because λ_{eq} is depth-dependent, it is taken into the spatial derivative on the right side of Eq. (8). Since the porosity of crustal rocks is typically small (~0.01-0.1), density and heat capacity are treated as constants, approximated using rock density and heat capacity.

A comprehensive model incorporating topography-driven flow and density-driven flow is inherently two- or three-dimensional. In this study, the rationales for using a 1D model include the following: (1) 1D model setup is the simplest approach addressing vertical exhumation of the rocks and how this process interacts with hydrothermal circulation and (2) the Nusselt number is used to represent the intensities and the thermal effects of hydrothermal circulation. Thus complex 2D or 3D flow patterns due to local topography and spatial distribution of magmatic heat sources can be avoided. The 1D model is intended to address generic first-order processes invoking conduction, exhumation, and hydrothermal circulation.

3.2. Permeability profile and penetration depth

Permeability decreases with depth due to the closure of pore spaces (e.g., Manning and Ingebritsen, 1999). In this study, we adopted the depth-dependent permeability ($k_\varphi(z)$) of Saar and Manga (2004), which was constrained by hydrological, thermal, seismic, and modeling studies in the Oregon Cascades to improve upon Manning and Ingebritsen (1999) (Fig. 2B):

$$k_\varphi(z) = \begin{cases} 5 \times 10^{-13}\ \mathrm{m}^2 \cdot \exp(\frac{-z}{0.25\ \mathrm{km}}) & 0 \le z \le 0.8\ \mathrm{km} \\ 10^{-14}\ \mathrm{m}^2 \cdot (\frac{z}{1\ \mathrm{km}})^{-3.2} & z > 0.8\ \mathrm{km} \end{cases} \tag{9}$$

We take $k_\varphi = 10^{-17}$ m^2 as the minimum permeability that allows for hydrothermal circulation to advect heat (Ingebritsen et al., 1992; Manning and Ingebritsen, 1999). Using the above permeability depth profile (Eq. (9)) yields a reference penetration depth (Z_{hyr}) of 8.66 km to which hydrothermal circulation is allowed to penetrate. We also note that below the brittle-ductile transition (BDT) depth, permeability is too low for fluids to advect heat (Manning and Ingebritsen, 1999). Thus, the penetration depth should not exceed the depth of the BDT. When the reference penetration depth is deeper than the BDT depth, the model forces the penetration depth (Z_{hy}) to match the BDT depth. The BDT depth in the model is defined by the depth of the 350 °C isotherm below which the quartz-dominated crust deforms plastically (e.g., Chen and Molnar, 1983). The initial BDT depth is 8.75 km, slightly deeper than the reference penetration depth.

We recognize that permeability is a dynamic property. The permeability structure evolves with the thermal state, porosity changes due to metamorphic reactions, and the crustal stress conditions related to regional tectonics. However, many of the controlling parameters, such as pore aspect ratio and pore space stiffness, are not constrained well enough to justify a more complicated permeability model.

3.3. Effective thermal conductivity

We used a simple approach similar to Roland et al. (2010) to link Nu and λ_{eq}. Nu decays exponentially with depth from a given surface value to $Nu = 1$ at the reference penetration depth Z_{hyr}, which results in the same exponential decay of λ_{eq} (Fig. 2C).

$$\lambda_{eq}(z) = \begin{cases} \lambda_0 \cdot Nu \cdot \exp(c_{hy} \cdot \frac{z}{Z_{hyr}}) & 0 \le z < Z_{hyr} \\ \lambda_0 & z \ge Z_{hyr} \end{cases} \tag{10}$$

where $c_{hy} = \ln(1/Nu)$ is a constant. When $Nu \to 1$, λ_{eq} becomes the normal thermal conductivity (λ_0), which is uniform with

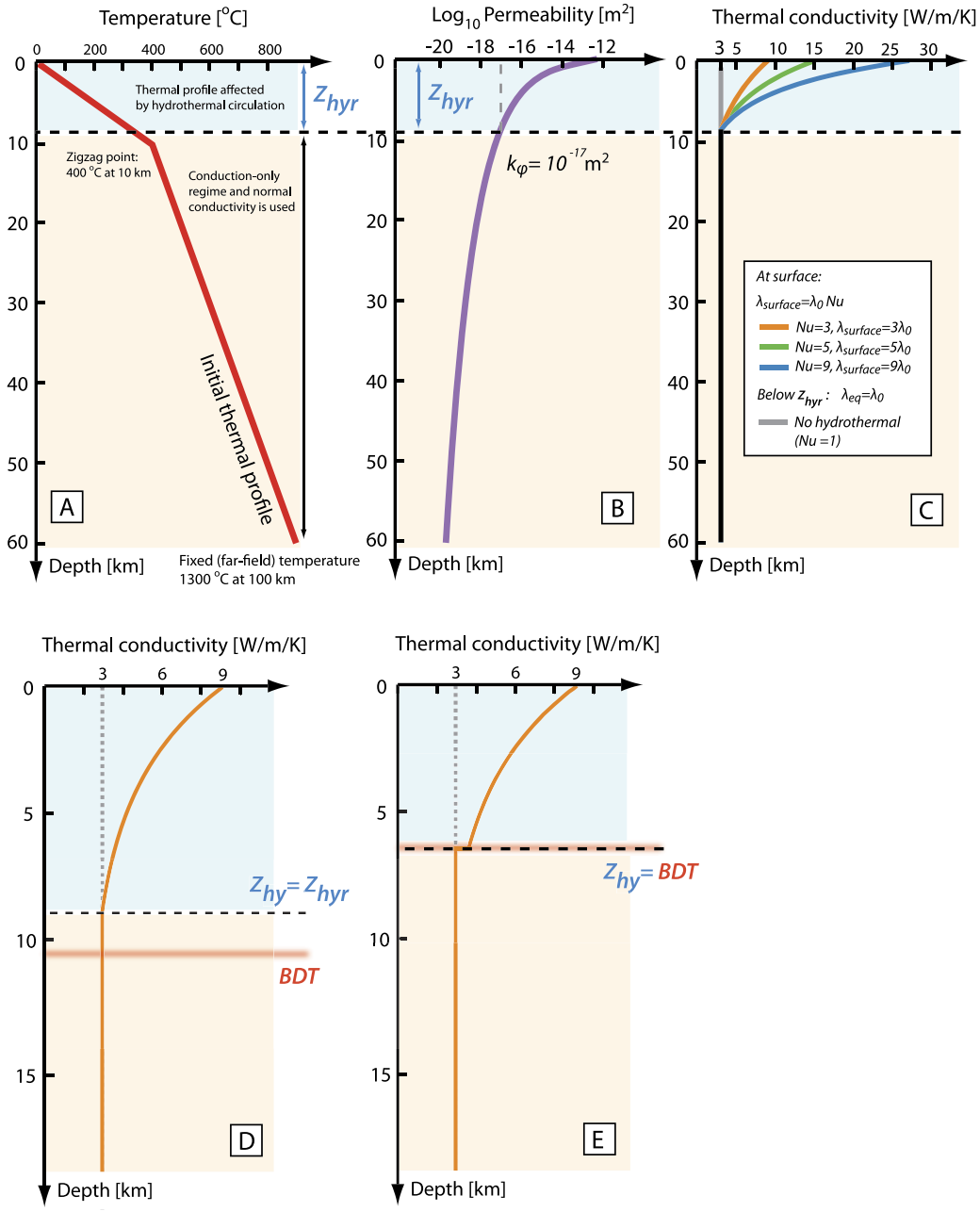

Fig. 2. Model setup showing (A) the initial thermal profile; (B) permeability profile used in the simulation (Eq. (9)); (C) thermal conductivity profiles corresponding to no hydrothermal circulation and hydrothermal circulation of different *Nu* numbers based on Eq. (10). The light blue area shows the regime where the thermal profile is affected by the hydrothermal circulation while the beige area shows the conduction-only regime. $k_\varphi = 10^{-17}$ m^2 is used as the minimum permeability that allows for hydrothermal circulation. Z_{hyr} is the reference penetration depth. $\lambda_{surface}$ is the thermal conductivity at the surface. (D) When the Brittle-Ductile Transition (BDT) depth is deeper than the reference penetration depth, penetration depth (Z_{hy}) equals Z_{hyr}. (E) When the BDT depth is shallower than Z_{hyr}, the model forces Z_{hy} to match the BDT depth.

depth. Additionally, λ_{eq} is assigned to λ_0 below the BDT depth (Fig. 2D, E). The exact range of the Nusselt number at surface in continental arcs is unknown, though it has been proposed to vary from 1 to 8 for hydrothermal systems in mid-ocean ridges (Roland et al., 2010). In an active continental arc with high precipitation such as the Oregon Cascades, the recharge-discharge rate (u_R) of groundwater is 0.5-1 m/yr (Saar and Manga, 2004). Using these rates, for a 20 °C temperature difference (ΔT) between the surface and ~500 m depth (Saar and Manga, 2004) and a near-surface porosity (ϕ) of 0.1 (Ingebritsen et al., 1992), the heat flux via groundwater flow is $\rho_f u_R C_{pf} \Delta T \phi \approx$ 130-260 mW/m^2 (ρ_f and C_{pf} are density and heat capacity of water). This value is several times higher than the mean background heat flux of 80-130 mW/m^2 in the deeper, conductive part of the crust (Saar and Manga, 2004). In the Oregon Cascades, heat transported by groundwater enhances, suppresses or even inverts ($dT/dz < 0$) near-surface temperature gradients in fluid discharge and recharge areas, respectively (Ingebritsen et al., 1989, 1992; Saar and Manga, 2004). These observations suggest hydrothermal heat transport strongly affects the total surface heat flux. To test a broad range of surface *Nu*, we vary its value from 1 (no hydrothermal circulation) to 9 (the most vigorous hydrothermal circulation).

3.4. Initial and boundary conditions

The size of the 1-D model represents a continental arc lithospheric column from the Earth's surface to the lithosphere-

asthenosphere boundary (LAB), which we place at 100 km, sufficiently far from the surface so we can focus only on surface processes in our thermal modeling. Surface temperature is fixed at 0 °C. LAB temperature is fixed at 1300 °C. We used a fixed-temperature bottom boundary condition, rather than a heat flux boundary because the LAB temperature is better constrained (Lee et al., 2009) than the basal heat flux in magmatic arcs. The fixed-temperature boundary condition also allows the surface heat flux to directly reflect the bulk thermal conductivity, whereas in the case of a basal heat flux boundary condition, the steady-state surface heat flux is ultimately controlled by the basal heat flux. To approximate the geothermal gradient of continental arcs constrained by metamorphic assemblages and mineral thermobarometry (Rothstein and Manning, 2003; Zhang et al., 2019), we adopted an initial thermal gradient of 40 °C/km in the top 10 km. Below 10 km, temperature increases in temperature from 400 °C to 1300 °C with a gradient of 10 °C/km (Fig. 2A). With this initial condition, the temperature at 60 km, a typical Moho depth in continental arcs, is a reasonable 900 °C.

3.5. Modeling techniques

We developed a 1-D finite-difference numerical model to solve Eq. (8). We assumed constant erosion rate (E) but varied its value in different simulations. In continental arcs, the typical peak surface erosion rate is about 1-2 km/Myr (Cao and Paterson, 2016; Jiang and Lee, 2017). It is noted that erosion rates much higher than 1-2 km/Myr are not uncommon in active mountain belts such as New Zealand Alps and Taiwan (Montgomery and Brandon, 2002). The erosion rate is not only controlled by elevation or topographic gradient, but it is also strongly influenced by climate conditions (e.g., annual precipitation) and bedrock erodibility. It is possible that continental arcs could have much higher erosion rates if the arcs locate in regions where annual precipitation and storm frequency are high. In order to test a broader range of erosion rate, we vary the erosion rate from 0 to 5 km/Myr.

To advect the temperature of rocks, we employed the marker-in-cell method to minimize numerical diffusion (e.g., Gerya, 2009). In our simulations, neither thermal conductivity nor permeability are advected with rocks. Our code can be easily modified to advect conductivity and permeability if needed. MATLAB scripts are presented in Supplementary Materials.

4. Simulation results

4.1. Evolution of thermal profiles

We tested different combinations of Nu and E, which vary from 1 to 9 and 0 to 5 km/Myr, respectively. Fig. 3 shows the thermal profiles of the reference simulation ($E = 2$ km/Myr and $Nu = 5$) compared with simulations without hydrothermal circulation. Hydrothermal circulation lowers the temperature and thermal gradient in the uppermost crust (Fig. 3A, B). When erosion is incorporated, hydrothermal circulation readily suppresses the increase of temperature in the uppermost crust caused by erosion (Fig. 3C, D).

We calculate the absolute temperature difference (ΔT) between the pure conduction case and the simulations with erosion and/or hydrothermal circulation (Fig. 4). When there is no hydrothermal circulation (Fig. 4 first row), erosion causes temperature to increase. When there is no erosion (Fig. 4 first column), hydrothermal circulation typically causes a temperature reduction of 50-100 °C in upper 15 km. The timing of maximum thermal reduction is achieved in 1-2 Myr, after which the perturbation is decreased.

When erosion and hydrothermal circulation are both involved, the change in temperature depends on the competing effects of hydrothermal circulation and advection. When the erosion rate is relatively slow (E = 1-2 km/Myr), hydrothermal cooling is capable of lowering the temperature for the first 5-10 Myr in the upper 10-15 km of crust (Fig. 4 B2-D2, B3-D3). When the erosion rate is fast ($E = 5$), moderate and intense hydrothermal circulation ($Nu = 5$ or 9) still reduces the temperature in the upper 10-15 km of the crust for the first 2 Myr (Fig. 4 C4, D4). If hydrothermal circulation is weak ($Nu = 3$), erosion overcomes hydrothermal circulation, resulting in the increase in temperature of the crust (Fig. 4 B4).

4.2. Total surface heat flux

Total surface heat flux is calculated using the product of the average geothermal gradient in the uppermost 500 m of the crust and the effective conductivity at 250 m depth. The total surface heat flux represents the integrated surface heat flux contributed by conduction, erosion and hydrothermal circulation. Fig. 5 shows the total surface heat flux derived from a series of simulations in which the values of Nu and E are varied. When hydrothermal circulation is active, total surface heat flux starts at a higher value than the conduction-erosion case, declines quickly within the first ~1-2 Myr (early stage), parallels and merges into the conduction-erosion heat flux afterwards (late stage). For a given erosion rate, hydrothermal circulation at higher Nu results in a higher total surface heat flux on both short (<~1-2 Myr) and long timescales.

4.3. Cooling rate of rock

We now examine the cooling rate of a rock as would be recorded by thermochronology. Fig. 6 shows the cooling paths of three parcels of rocks with initial temperatures of 700 °C, 500 °C, and 300 °C. When there is no erosion ($Nu = 1$), hydrothermal circulation increases the cooling rate (Fig. 6A). When erosion occurs, the time required to cool a parcel of rock from its initial temperature to the surface temperature of 0 °C depends on the initial temperature (initial depth) and the erosion rate (Fig. 6B-D). Therefore, for a given E, the average cooling rates from the initial temperature to 0 °C are the same for different Nu.

The exact cooling path depends on Nu. A useful parameter to characterize the cooling path is the time required to reach half of the initial temperature of T_0 ($t_{1/2}^{T_0}$). For example, for $E = 3$ km/Myr case, $t_{1/2}^{500}$ are 5.0 ($Nu = 1$), 3.9 ($Nu = 3$), 3.6 ($Nu = 5$), and 3.3 Myr ($Nu = 9$) (Fig. 6D). Increasing Nu corresponds to decreasing $t_{1/2}^{T_0}$. Hydrothermal circulation also tends to increase the cooling rate of rock parcels having lower initial temperature, which could particularly affect the interpretations of low-temperature thermochronological systems. This is discussed further in Section 5.2.

4.4. Rheological evolution of a cooling crust

Fig. 7 shows yield strength envelopes of the upper 25 km crust. The brittle strength profile is based on the Byerlee's law for strike-slip faulting. The viscous flow strength is based on wet-quartzite rheology (Ranalli, 1995) under a strain rate of 10^{-15} s^{-1}. For pure conduction, the depth of the brittle-ductile transition deepens and the area of yield strength envelope increases with time. With hydrothermal circulation, the depth of brittle-ductile transition occurs about 3 km deeper than the depth in the pure conduction case after 10 Myr (Fig. 7A, B). When erosion is incorporated, hydrothermal circulation is still able to maintain the brittle-ductile transition at a greater depth (Fig. 7D, F) compared to the case without hydrothermal circulation (Fig. 7C, E). For a

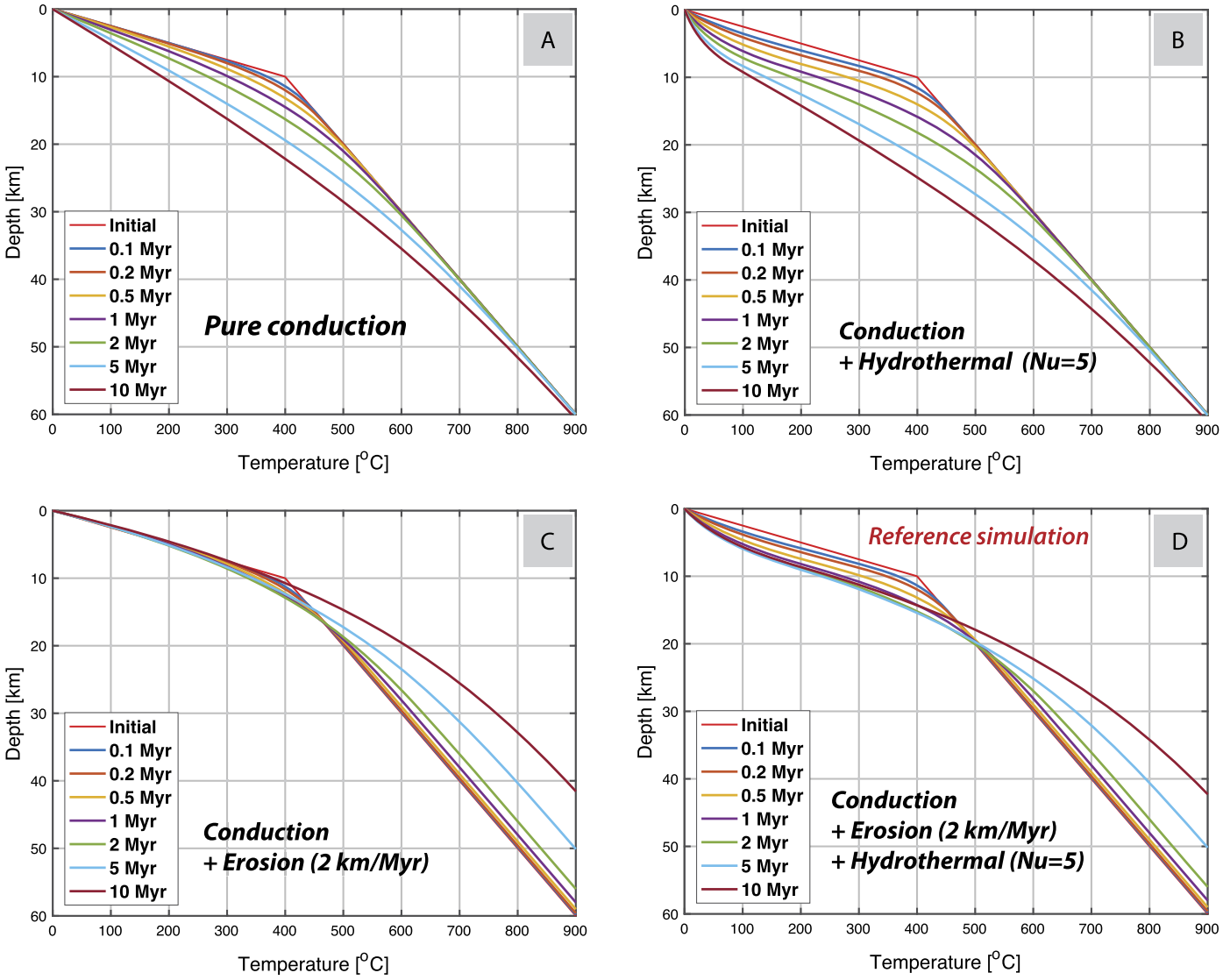

Fig. 3. Simulated thermal profiles from (A) pure conduction; (B) conduction with hydrothermal circulation ($Nu = 5$); (C) conduction with 2 km/Myr erosion; (D) reference simulation in which conduction, 2 km/Myr erosion, and hydrothermal circulation ($Nu = 5$) occur simultaneously.

crust with quartz-controlled rheology, the brittle-ductile transition can also be approximated by the 350 °C isotherm. Fig. 8 shows that when hydrothermal circulation is effective, the 350 °C isotherm-defined brittle-ductile transition deepens relative to the conduction-erosion cases.

5. Discussion

5.1. Hydrothermal circulation cools continental crust under exhumation

Cooling of continental crust by different processes can be quantified by evaluating how those processes contribute to the total surface heat flux. Let $\overline{\lambda}$ and $\overline{\kappa}$ be the bulk average thermal conductivity and diffusivity ($\overline{\kappa} = \overline{\lambda}/(\rho C_p)$) of the cooling crust or lithosphere. For a bulk layer containing multiple stratified layers of variable conductivity, $\overline{\lambda}$ can be calculated (Jaupart and Mareschal, 2010, Eq. 4.33):

$$\overline{\lambda} = \left\{ \frac{1}{L} \int_0^L \frac{dz}{\lambda_{eq}(z)} \right\}^{-1} \tag{11}$$

When $L \geq Z_{hyr}$, inserting Eq. (10) into Eq. (11) and integrating, we have:

$$\overline{\lambda} = \lambda_0 \cdot \left\{ \frac{Nu - 1}{Nu} \cdot \frac{1}{\ln(Nu)} \cdot f + (1 - f) \right\}^{-1} \tag{12}$$

f is the ratio of the thickness of the hydrothermal layer to the thickness of the crustal-lithospheric column whose upper and bottom temperatures are fixed:

$$f = \frac{Z_{hyr}}{L} \tag{13}$$

If there is no erosion, the steady-steady total heat flux from simultaneous conduction and hydrothermal circulation (q_{CH}) should be proportionally increased by a factor of γ ($\gamma = \overline{\lambda}/\lambda_0$) compared to q_C: $q_{CH} = q_C \cdot \gamma$. Fig. 9A shows how γ increases with increasing f and Nu. Corresponding characteristic time (τ_{CH}), and steady state geothermal gradient can be calculated (Table 1). Since $\overline{\lambda}$ introduces hydrothermal layer, we have $\overline{\lambda} > \lambda_0$, $\overline{\kappa} > \kappa_0$, and $\tau_{CH} < \tau_C$, suggesting that hydrothermal circulation reduces the characteristic time and thus promotes cooling. In our simulation, since the f is small (~0.1), γ is only slightly higher than 1. For the $Nu = 9$ case, γ is about 1.05. This results in the slight higher long-term

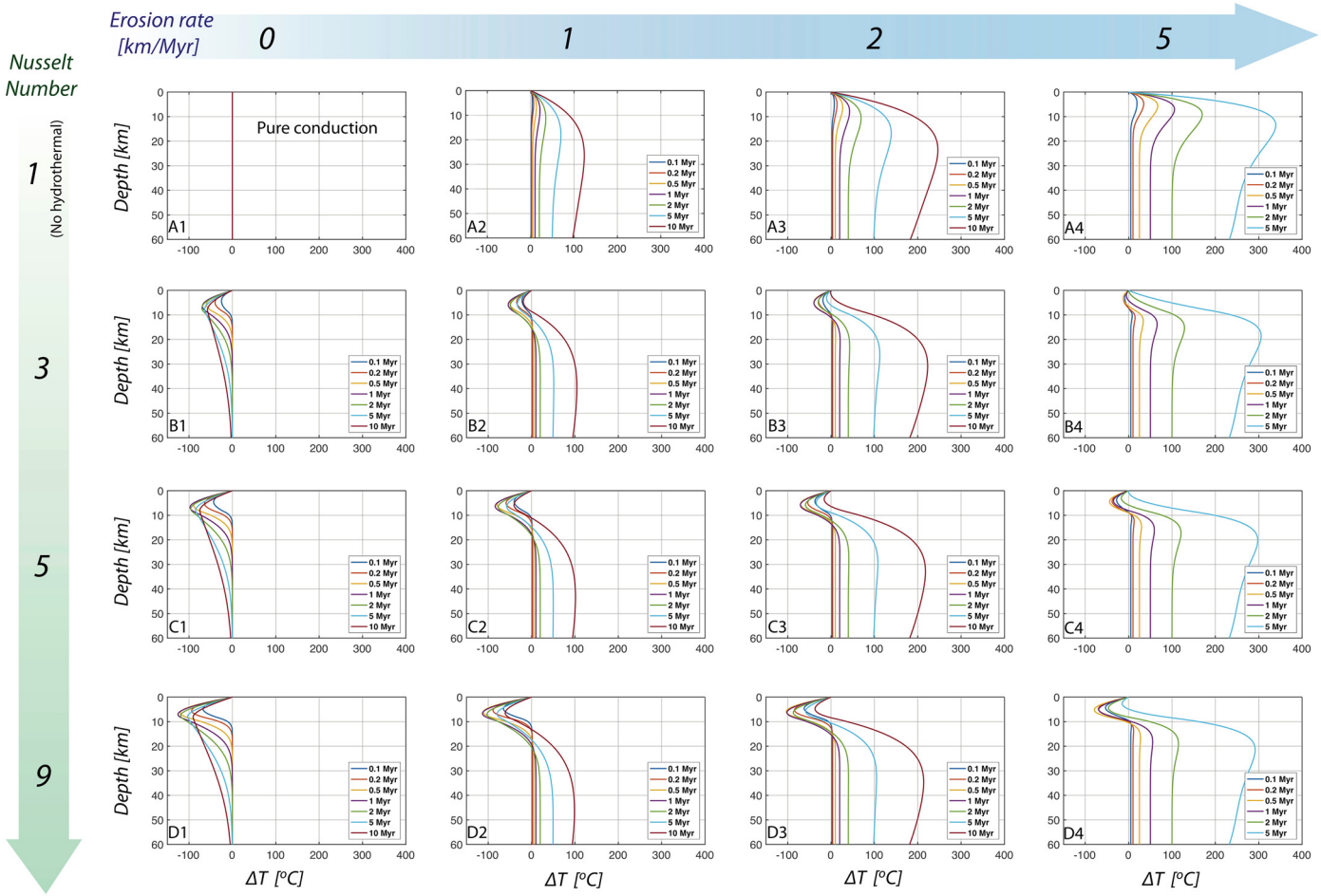

Fig. 4. Absolute temperature difference (ΔT) relative to the purely conductive thermal profile for simulations of different combinations of erosion rate and Nusselt number.

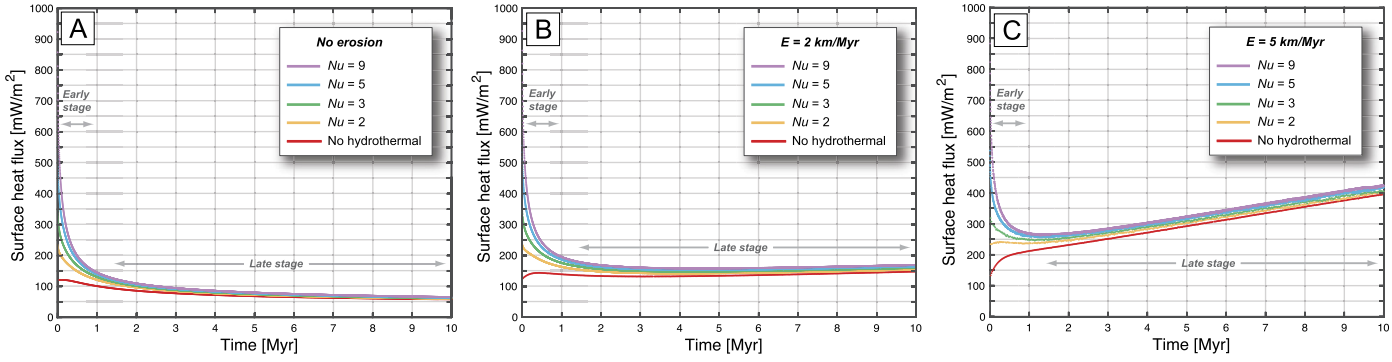

Fig. 5. Evolution of total surface heat flux resulting from combinations of different erosion rates and Nusselt numbers.

surface heat flux (when $Nu > 1$) comparing to conductive heat flux (Fig. 5A).

When erosion is additionally incorporated, we define the modified Péclet number (Pe') using $\overline{\kappa}$ since hydrothermal circulation has been effectively incorporated. And the characteristic time for simultaneous conduction, erosion and hydrothermal circulation (τ_{CEH}) can also be derived:

$$Pe' = \frac{EL}{\overline{\kappa}} = \frac{Pe}{\gamma} \tag{14}$$

$$\tau_{CEH} = \frac{L^2}{\overline{\kappa}(1 + Pe')} \tag{15}$$

Numerical simulations show (Fig. 5) that when erosion and hydrothermal circulation both occur, the total surface heat flux of shows two-stage characteristics: a higher value at early stage, dropping quickly within 0.5-2 Myr, with the total surface heat flux paralleling and eventually merging into the heat flux of conduction and erosional advection at longer times (late stage). The timescale to transition to late stage (τ_T) can be calculated using Eq. (15) by letting $L = 10$ km and $\overline{\kappa}$ be the average thermal diffusivity in the uppermost 10 km crust. For the total surface heat flux evolutions shown in Fig. 5A, B and C (except $Nu = 2$, the yellow curve in Fig. 5C), we have $Pe' < 1$ and τ_{CEH} of the uppermost 10 km crust ranges from 0.3 to 2.1 Myr, which is consistent with simula-

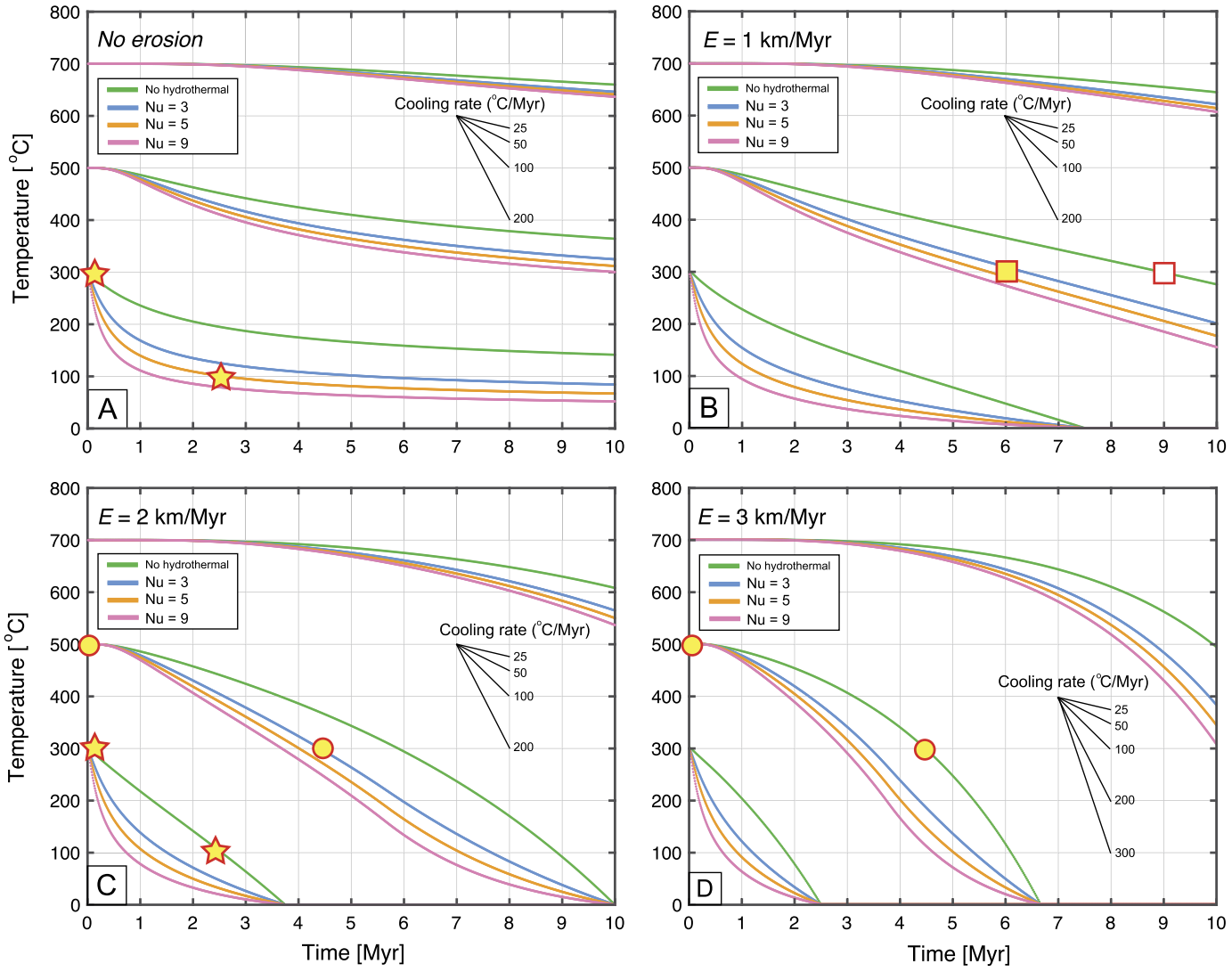

Fig. 6. Cooling histories of tracked parcels of rocks with different erosion rates and intensities of hydrothermal circulation. The initial temperatures are 300 °C, 500 °C, and 700 °C. Colors denote different Nusselt numbers. Filled stars in (A) and (C) show two similar average cooling rates from 300 °C to 100 °C. Filled circles in (C) and (D) show two similar average cooling rates from 500 °C to 300 °C. Squares in (B) illustrate different cooling times from 500 °C to 300 °C with (filled square) and without (open square) hydrothermal circulation.

tion results. When the erosion rate is fast enough to cause $Pe' > 1$, the system reaches late stage quickly without a decrease of surface heat flux (yellow curve in Fig. 5C). The initial total surface heat flux (q_i) can be calculated as follows:

$$q_i = \Gamma_i \cdot \lambda_0 \cdot Nu \tag{16}$$

where Γ_i is the initial geothermal gradient at the surface. Although the early-stage evolution of total surface heat flux is transient and the initial total surface heat flux is affected by the initial geothermal gradient, these results illustrate that when hydrothermal circulation starts, the upper crust is characterized by short-lived, intense heat dissipation. Not surprisingly, more vigorous hydrothermal circulation and a hotter crust lead to higher surface heat flux and faster cooling.

The steady-state ($t \gg \tau_{CEH}$) total surface heat flux of simultaneous conduction, erosion, and hydrothermal circulation (q_{CEH}) can also be calculated. Similar to Eq. (4), replacing q_{CH} with q_C and Pe with Pe', and knowing that $q_{CH} = q_C \cdot \gamma$, and γ is a function of Nu and f (Eq. (12)):

$$q_{CEH} = q_C \cdot \frac{Pe'}{1 - \exp(-Pe')} \cdot \gamma(Nu, f) \tag{17}$$

Eq. (17) explicitly shows how erosion and hydrothermal circulation modulate the steady-state conductive surface heat flux, and how the total surface heat flux is controlled by two dimensionless numbers: Pe' or Pe, and γ (knowing $Pe' = Pe/\gamma$). When $Pe' \gg 3$ (or $Pe \gg 3\gamma$), $Pe' \simeq Pe'/(1 - \exp(-Pe'))$, the above equation becomes:

$$q_{CEH} \simeq q_C \cdot Pe \tag{18}$$

Eq. (18) shows when Pe is large enough, q_{CEH} approaches the state-steady conduction-erosional advection heat flux (q_{CE}). Fig. 9B shows how normalized surface heat flux changes with Pe and γ. In our simulations, the Pe is large ($Pe \simeq 3$ if $E = 1$ km/Myr) due to the large lithospheric thickness used. Consequently, Figs. 5B, 5C show that q_{CEH} approaches q_{CE} during the late stage evolution.

Finally, we can calculate the steady-state thermal profile with hydrothermal circulation. At steady state, the heat flux is constant with depth:

$$\lambda_{eq}(z) \cdot T'(z) = q_{CEH} \tag{19}$$

$T'(z)$ is the thermal gradient at a depth of z. Using Eqs. (17) and (19), we have:

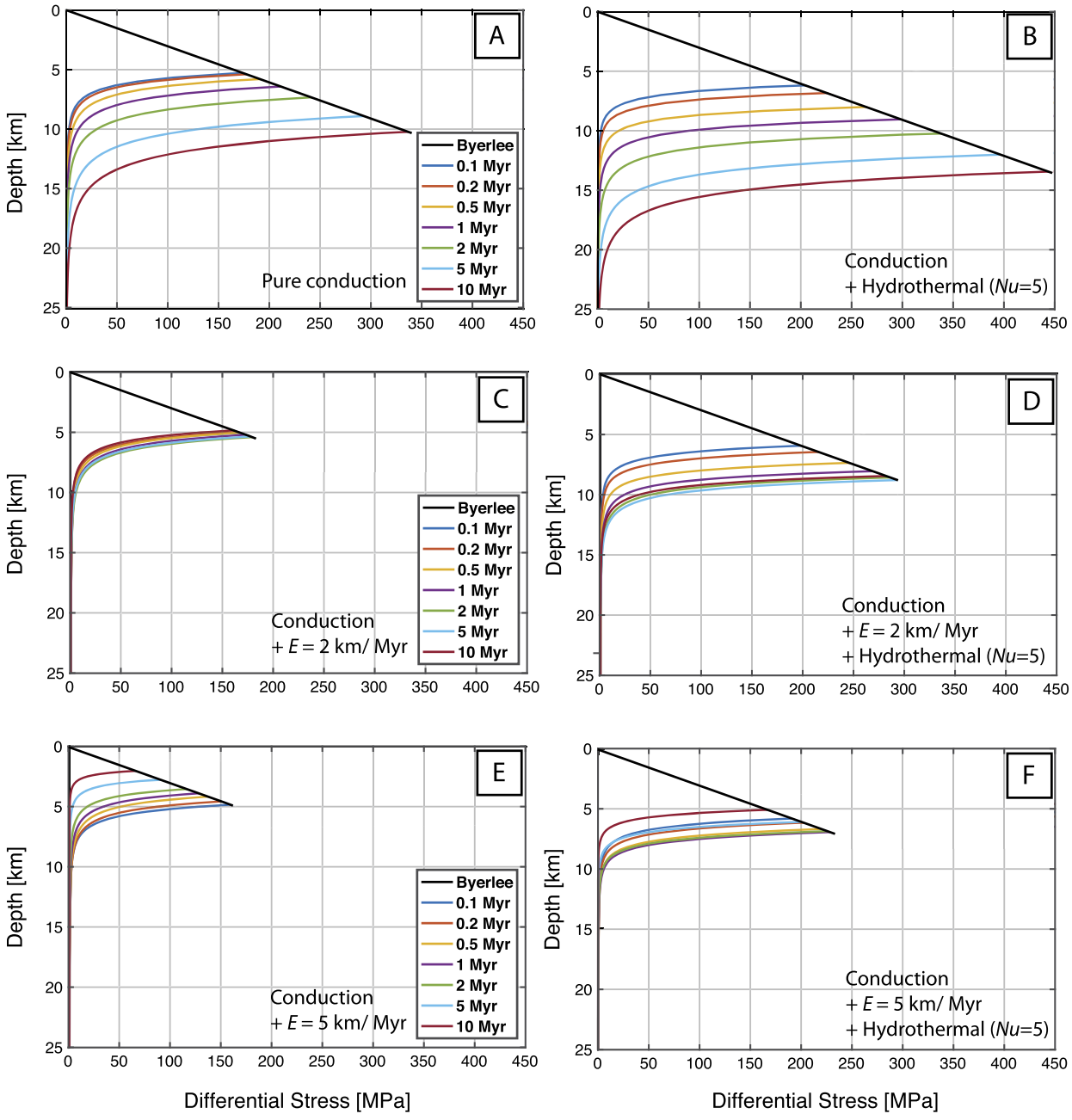

Fig. 7. Temporal evolutions of yield strength envelopes in the upper crust responding to erosion and hydrothermal circulation. The black line represents Byerlee's law in a strike-slip faulting regime. Wet-quartzite rheology (Ranalli, 1995) is used to construct the flow strength profiles and strain rate of 10^{-15} s^{-1} is used.

$$T(z) = T_S + \int_0^z \frac{\overline{\lambda} \cdot \Gamma}{\lambda_{eq}(z)} \cdot \frac{Pe' \cdot dz}{1 - \exp(-Pe')} \tag{20}$$

Based on simulations and scaling analysis, we find that: (1) hydrothermal circulation amplifies the surface heat flux of simultaneous conduction and erosion, resulting in a persistent cooling effect, (2) more vigorous hydrothermal circulation leads to larger *Nu*, and f increases when the hydrothermal layer occupies a greater portion between two thermal boundaries. γ increases as *Nu* and f and increase. For a thin crust (e.g., $L = 25$ km) and the same penetration depth, $\gamma = 1.23$ when $Nu = 5$, which means hydrothermal circulation could increase surface heat flux up to ~20% when $Pe' < 3$. Therefore, the relative thickness of hydrothermal layer is an important factor affecting surface heat flux, and (3) erosional advection provides a larger surface heat flux baseline for the heat dissipation by hydrothermal circulation but faster erosion can also diminish the long-term hydrothermal cooling effect. The hydrothermal cooling at steady state is more effective when *Pe* is small (Fig. 9B). Although only erosional advection is discussed in this study, tectonic processes can also advect rocks toward the surface. The Basin and Range Province, where tectonic extension and crustal thinning advect hot crust upwards, is an example. In such a case, if the penetration depth and *Nu* remain constant, f will increase during crustal thinning, resulting in more efficient heat loss through time.

In this study, the increase in thermal gradient is caused by erosion-induced advection. Other processes can also increase thermal gradients, including magmatism in active arcs and tectonic denudation. Magmatism can provide strong heat sources within the crust enhancing the density-driven flow.

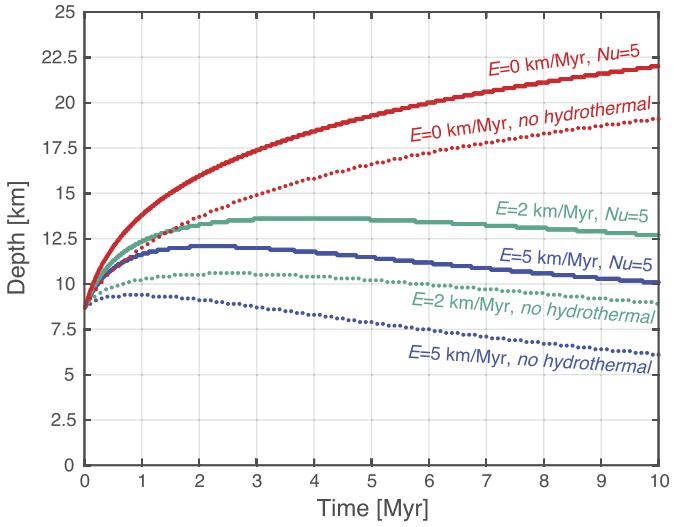

Fig. 8. Depth of 350 °C isotherm, representing the depth of brittle-ductile transition, evolving with time. Results for erosion rates of 0 (red), 2 (green), and 5 (blue) km/Myr with and without hydrothermal circulation are shown.

5.2. Effects on the interpretation of thermochronological data

Hydrothermal circulation affects the interpretation of thermochronological data. A faster average cooling rate can be interpreted as either the result of erosion or the result of hydrothermal cooling. For example, for the simulated continental crust in this study, cooling from 300 °C to 100 °C (at the rate of 80 °C/Myr) can be explained by either erosion of 2 km/Myr (Fig. 6C, filled star markers) or hydrothermal circulation at $Nu = 3$ without any erosion (Fig. 6A, filled star markers). A faster average cooling rate can also be interpreted as a combination of slower erosion and additional hydrothermal cooling. Conductive-advective cooling from 500 °C to 300 °C (approximately the hornblende and biotite $^{40}Ar/^{39}Ar$ closure temperatures, respectively) takes about 4.5 Myr when the erosion rate is 3 km/Myr (Fig. 6D, filled circle markers). The same cooling rate can be with slower erosion of 2 km/Myr and hydrothermal circulation at $Nu = 5$ (Fig. 6C, filled circle markers).

Varying thermal conductivity due to lithology and its effect on low-temperature thermochronological data have been discussed (e.g., Braun et al., 2016; Łuszczak et al., 2017). Many of these studies assume an increase of thermal conductivity from the sedimentary cover (0.5-2.5 W/m/K) to crystalline basement (1.5-3.5 W/m/K), so that the sediments serve as an "insulating" layer (e.g., Braun et al., 2016; Łuszczak et al., 2017). Exhumation of these "insulating layers" causes over-estimation of cooling rate. In contrast, Braun et al. (2016) noted that if the conductivity profile is a "static" function of depth and is not advected with rocks as the model setup in this study, decrease or increase of thermal conductivity with depth could lead to over-estimation or under-estimation of the exhumation rate, respectively. This conclusion is consistent with our simulations.

5.3. Model limitations

We adapted the static permeability structure from Saar and Manga (2004) and thus ignored the dynamic processes of establishment of hydrothermal circulation. If the timescale to establish hydrothermal circulation is comparable to or even greater than the timescale of thermal diffusion, the initial surface flux simulated should be dampened or smoothed. When calculating the of the strength of the upper crust, we only considered the thermal effect. In the ductile regime, the involvement of water may reduce flow strength (e.g., Stipp et al., 2006). Thus, the yield strength envelopes shown in Fig. 7 represent the maximum strength. Future studies might consider incorporating the dynamics of hydrothermal circulation by using time-dependent permeability and self-adaptive effective thermal conductivity (e.g., Schmeling and Marquart, 2014). In active arcs, one could parameterize magmatic heating using geologically constrained magmatic flux (e.g., Paterson and Ducea, 2015).

5.4. Geological relevance

Several lines of field, isotopic, and thermochronological evidence suggest that hydrothermal circulation was active in the upper crust in the Late Cretaceous Sierra Nevada Arc. Hydrothermal activity is recorded as extensive quartz vein networks in a 90-70 Ma brittle-ductile transpressional shear zone in the Sawmill Canyon area in eastern central Sierra Nevada (Compton et al., 2017; Hartman et al., 2018). Oxygen and hydrogen isotopic ratios of the quartz veins suggest incursion of meteoric-hydrothermal fluids at a depth of 2-3 kbars (Compton et al., 2017; Hartman et al., 2018). In the southeast Sierra Nevada foothills, hydrothermal activity is recorded by the altered ~100 Ma granitic rocks, which

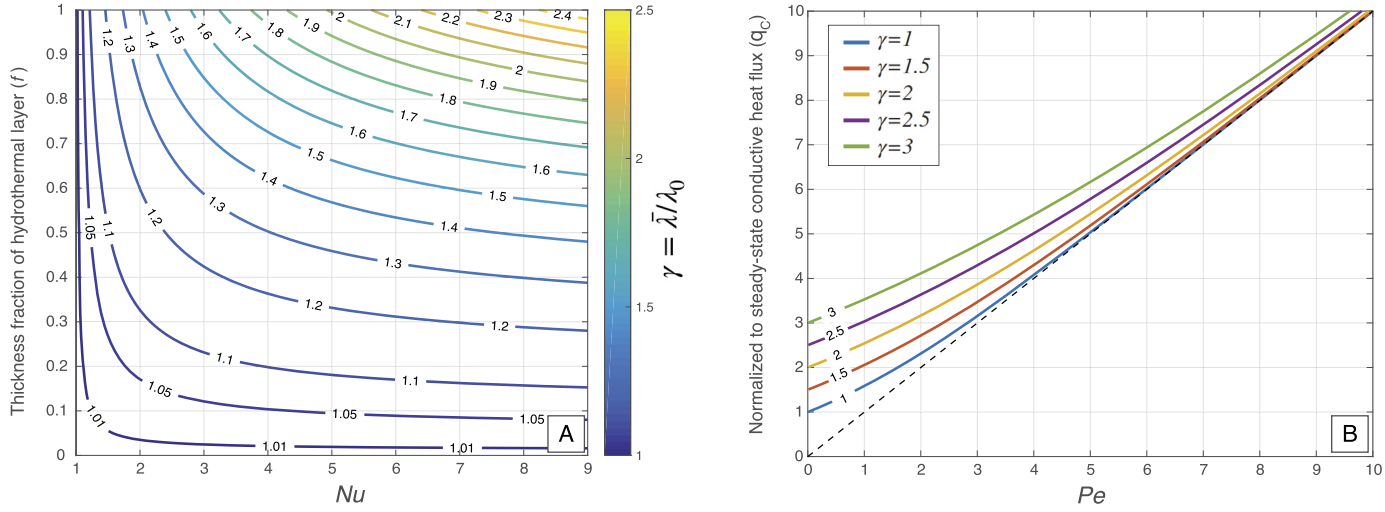

Fig. 9. (A) Variation in γ (ratio of bulk average thermal conductivity $\bar{\lambda}$ to normal thermal conductivity λ_0) as a function of Nusselt number (Nu) at surface and the thickness fraction (f) of the hydrothermal layer relative to the crust or lithosphere. (B) Surface heat flux normalized to steady-steady conductive heat flux as a function of Péclet number (Pe) and γ. When $\gamma = 1$, there is no hydrothermal circulation. The dashed line represents the asymptote when Pe is large.

hosts an assemblage of retrograded minerals including quartz, plagioclase, calcite, anatase, chlorite, and brookite (Sousa et al., 2017). Sousa et al. (2017) suggested $\delta^{18}O$ values, intergrowth texture, and ~100 °C crystallization temperature of the calcite represent meteoric fluid interaction during tectonic exhumation of the southern Sierra Nevada at 95-85 Ma (e.g., Chapmen et al., 2012). These isotopic signatures of meteoric fluids suggest effective advection of oxygen isotopes occurred at the BDT depth or the lower upper–middle crust where permeability is too low ($<10^{-18}$ m^2) for significant heat advection (Manning and Ingebritsen, 1999). Nonetheless, heat advection through hydrothermal circulation could still be efficient in the shallower depth in these regions, which aids the cooling of the arc and facilitates brittle deformation.

More direct evidence of hydrothermal cooling comes from thermochronological ages. Compilation of regional hornblende and biotite $^{40}Ar/^{39}Ar$ cooling ages suggests that the east-central Sierra Nevada cooled from hornblende to biotite closure temperatures (~530 to ~330 °C) within 5.7 to 6.7 Myr at a relatively fast average rate of ~30-35 °C/Myr during the Late Cretaceous (Nadin et al., 2016). The erosion rate in the Late Cretaceous Sierra Nevada constrained by low-temperature thermochronology (Cecil et al., 2006) and mass balance-isostasy modeling (Lee et al., 2015; Cao and Paterson, 2016) ranges from 0.2-1 km/Myr. Thermal modeling using reasonable arc crust geothermal gradients and only conduction-advection cannot reproduce the observed cooling rate and timespan even if the upper bound of erosion rate (constant 1 km/Myr) is used (open square in Fig. 6B representing 9-Myr cooling timespan from 500 to 300 °C). One possible way to speed up cooling rates is to have additional hydrothermal circulation (filled square in Fig. 6B representing 6-Myr cooling timespan from 500 to 300 °C).

In the southern Sierra Nevada Batholith, rapid regional cooling between ~97-82 Ma is exemplified by the nearly identical hornblende and biotite $^{40}Ar/^{39}Ar$ ages of 91 Ma in the west Isabella Lake area (Nadin et al., 2016). We suggest that such rapid cooling might have been aided by hydrothermal circulation, in addition to tectonic exhumation of southern Sierra Nevada. Fast cooling could have facilitated the transition from a ductile proto-Kern Canyon shear zone to the brittle Kern-Canyon at about 85 Ma in the southern Sierra Nevada (Nadin et al., 2016). The hydrothermal activity in the Sawmill Canyon area may also have facilitated the transition from ductile shearing to brittle faulting around 80 Ma (e.g., Cao et al., 2015; Hartman et al., 2018).

Hydrothermal activity may play an important role in regulating thermal and rheological structures in the Basin and Range Province, where relatively fast tectonic denudation occurs in thin and hot continental crust (e.g., Dickinson, 2006). Magmatic fluid supplied by the extensive Cenozoic plutonism provide the source for circulation in addition to the meteoric water. $^{40}Ar/^{39}Ar$ ages and hydrogen isotopes in syn-kinematic mica from the northern Snake Range core complex suggest that meteoric water was able to circulate from the surface to the brittle-ductile transition depth across the detachment for 6 Myr (Gébelin et al., 2015). Hydrothermal cooling could have promoted brittle faulting along the detachment and thus facilitated the initial extension. The resulting crustal thinning promotes faster cooling not only by exhumation itself but also by increasing the cooling efficiency of hydrothermal circulation via increasing relative thickness of the hydrothermal layer. The thinned crust with hydrothermal cooling in effect may act to suppress extension-related volcanism (Gans and Bohrson, 1998). A negative feedback may develop through strengthening of the crust by faster cooling, leading to the cessation of rapid extension.

6. Conclusions

Although hydrothermal circulation is limited to the top several kilometers, it plays an important role in cooling hot continental crust and regulating thermal and rheological structures. Simulations and scaling analyses demonstrate that hydrothermal cooling lowers the thermal gradient in the upper crust, increases cooling rates of exhuming crust, and forces the brittle-ductile transition towards greater depth during erosion. Hydrothermal circulation imposes intense short-term and persistent long-term cooling effects on exhuming crust via increasing the total surface heat flux. Particularly, hydrothermal cooling at steady steady is more effective when Péclet number is small. Interpretation of low-temperature thermochronological data could overestimate average cooling rate if the effect of hydrothermal circulation is not considered.

Acknowledgements

This study is supported by the United States National Science Foundation (NSF) awarded (OCE-1338842) to Lee and NSF awarded (EAR-1830139) to Zuza and Cao. We thank Steve Ingebritsen and an anonymous reviewer for their critical comments that improved the quality of the manuscript. Editor Rebecca Bendick is thanked for the efficient handling of the submission. Cao also thanks Scott Tyler for scientific discussion.

Appendix A. Supplementary material

Supplementary material related to this article can be found online at https://doi.org/10.1016/j.epsl.2019.03.029.

References

Allmendinger, R.W., Jordan, T.E., Kay, S.M., Isacks, B.L., 1997. The evolution of the Altiplano-Puna plateau of the Central Andes. Annu. Rev. Earth Planet. Sci. 251, 139–174. https://doi.org/10.1146/annurev.earth.25.1.139.

Batt, E., Brandon, M.T., 2002. Lateral thinking: 2-D interpretation of thermochronology in convergent orogenic settings. Tectonophysics 349, 185–201. https://doi.org/10.1016/S0040-1951(02)00053-7.

Braun, J., Stippich, C., Glasmacher, U.A., 2016. The effect of variability in rock thermal conductivity on exhumation rate estimates from thermochronological data. Tectonophysics, 1–10. https://doi.org/10.1016/j.tecto.2016.09.027.

Braun, J., Van Der Beek, P., Valla, P., Robert, X., Herman, F., Glotzbach, C., Pedersen, V., Perry, C., Simon-Labric, T., Prigent, C., 2012. Quantifying rates of landscape evolution and tectonic processes by thermochronology and numerical modeling of crustal heat transport using PECUBE. Tectonophysics 524, 1–28. https://doi.org/10.1016/j.tecto.2011.12.035.

Cao, W., Paterson, S.R., Memeti, V., Mundil, R., Anderson, J.L., Schmidt, K., 2015. Tracking paleodeformation fields in the Mesozoic central Sierra Nevada arc: implications for intra-arc cyclic deformation and arc tempos. Lithosphere 7, 296–320. https://doi.org/10.1130/L389.1.

Cao, W., Paterson, S.R., 2016. A mass balance and isostasy model: exploring the interplay between magmatism, deformation, and surface erosion in continental arcs using central Sierra Nevada as a case study. Geochem. Geophys. Geosyst., 1–19. http://doi.org/10.1002/2015GC006229.

Cathles, L.M., 1977. An analysis of the cooling of intrusives by ground-water convection which includes boiling. Econ. Geol. 72, 804–826. https://doi.org/10.2113/gsecongeo.72.5.804.

Cecil, M.R., Ducea, M.N., Reiners, P.W., Chase, C.G., 2006. Cenozoic exhumation of the northern Sierra Nevada, California, from (U-Th)/He thermochronology. Geol. Soc. Am. Bull. 118, 1481–1488. https://doi.org/10.1130/B25876.1.

Chapman, A.D., Saleeby, J.B., Wood, D.J., Piasecki, A., Kidder, S., Ducea, M.N., Farley, K.A., 2012. Late Cretaceous gravitational collapse of the southern Sierra Nevada batholith, California. Geosphere 8 (2), 314–341. https://doi.org/10.1130/GES00740.1.

Chen, W.P., Molnar, P., 1983. Focal depths of intracontinental and intraplate earthquakes and their implications for the thermal and mechanical properties of the lithosphere. J. Geophys. Res., Solid Earth 88 (B5), 4183–4214. https://doi.org/10.1029/JB088iB05p04183.

Compton, K.E., Kirkpatrick, J.D., Holk, G.J., 2017. Cyclical shear fracture and viscous flow during transitional ductile-brittle deformation in the Saddlebag Lake Shear Zone, California. Tectonophysics 708, 1–14. https://doi.org/10.1016/j.tecto.2017.04.006.

Diamond, L.W., Wanner, C., Waber, H.N., 2018. Penetration depth of meteoric water in orogenic geothermal systems. Geology 46, 1063–1066. https://doi.org/10.1130/G45394.1.

Dickinson, W.R., 2006. Geotectonic evolution of the Great Basin. Geosphere 2 (7), 353–368. https://doi.org/10.1130/GES00054.1.

Fekete, S., Weis, P., Driesner, T., Bouvier, A.-S., Baumgartner, L., Heinrich, C.A., 2016. Contrasting hydrological processes of meteoric water incursion during magmatic-hydrothermal ore deposition: an oxygen isotope study by ion microprobe. Earth Planet. Sci. Lett. 451, 263–271. https://doi.org/10.1016/j.epsl.2016.07.009.

Gans, P.B., Bohrson, W.A., 1998. Suppression of volcanism during rapid extension in the Basin and Range Province, United States. Science 279 (5347), 66–68.

Gébelin, A., Teyssier, C., Heizler, M.T., Mulch, A., 2015. Meteoric water circulation in a rolling-hinge detachment system (northern Snake Range core complex, Nevada). Geol. Soc. Am. Bull. 127 (1–2), 149–161. https://doi.org/10.1130/B31063.1.

Gerya, T., 2009. Introduction to Numerical Geodynamic Modelling. Cambridge University Press.

Hartman, S.M., Paterson, S.R., Holk, G.J., Kirkpatrick, J.D., 2018. Structural and hydrothermal evolution of a strike-slip shear zone during a ductile-brittle transition, Sierra Nevada, CA. J. Struct. Geol. 113, 134–154. https://doi.org/10.1016/j.jsg.2018.05.010.

Hayba, D.O., Ingebritsen, S.E., 1997. Multiphase groundwater flow near cooling plutons. J. Geophys. Res., Solid Earth 102 (B6), 12235–12252. https://doi.org/10.1029/97JB00552.

Ingebritsen, S.E., Sherrod, D.R., Mariner, R.H., 1989. Heat-flow and hydrothermal circulation in the Cascade range, north-central Oregon. Science 243, 1458–1462. https://doi.org/10.1126/science.243.4897.1458.

Ingebritsen, S.E., Sherrod, D.R., Mariner, R.H., 1992. Rates and patterns of groundwater flow in the Cascade Range volcanic arc, and the effect on subsurface temperatures. J. Geophys. Res., Solid Earth 97 (B4), 4599–4627. https://doi.org/10.1029/91JB03064.

Ingebritsen, S.E., Geiger, S., Hurwitz, S., Driesner, T., 2010. Numerical simulation of magmatic hydrothermal systems. Rev. Geophys. 48 (1). https://doi.org/10.1029/2009RG000287.

Jaupart, C., Mareschal, J.C., 2010. Heat Generation and Transport in the Earth. Cambridge University Press.

Jiang, H., Lee, C.-T.A., 2017. Coupled magmatism–erosion in continental arcs: reconstructing the history of the Cretaceous Peninsular Ranges batholith, southern California through detrital hornblende barometry in forearc sediments. Earth Planet. Sci. Lett. 472, 69–81. https://doi.org/10.1016/j.epsl.2017.05.009.

Kooi, H., 2016. Groundwater flow as a cooling agent of the continental lithosphere. Nat. Geosci., 1–5. https://doi.org/10.1038/ngeo2642.

Lee, C.-T.A., Luffi, P., Plank, T., Dalton, H.A., Leeman, W.P., 2009. Constraints on the depths and temperatures of basaltic magma generation on Earth and other terrestrial planets using new thermobarometers for mafic magmas. Earth Planet. Sci. Lett. 279, 20–33. https://doi.org/10.1016/j.epsl.2008.12.020.

Lee, C.-T.A., Thurner, S., Paterson, S.R., Cao, W., 2015. The rise and fall of continental arcs: interplays between magmatism, uplift, weathering, and climate. Earth Planet. Sci. Lett. 425, 105–119. https://doi.org/10.1016/j.epsl.2015.05.045.

Łuszczak, K., Persano, C., Braun, J., Stuart, F.M., 2017. How local crustal thermal properties influence the amount of denudation derived from low-temperature thermochronometry. Geology 45, 779–782. https://doi.org/10.1130/G39036.1.

Manga, M., 1998. Advective heat transport by low-temperature discharge in the Oregon Cascades. Geology 26, 799–802. https://doi.org/10.1130/0091-7613(1998)026<0799:AHTBLT>2.3.CO;2.

Manning, C.E., Ingebritsen, S.E., 1999. Permeability of the continental crust: implications of geothermal data and metamorphic systems. Rev. Geophys. 37, 127–150. https://doi.org/10.1029/1998RG900002.

Montgomery, D.R., Brandon, M.T., 2002. Topographic controls on erosion rates in tectonically active mountain ranges. Earth Planet. Sci. Lett. 201, 481–489. https://doi.org/10.1016/S0012-821X(02)00725-2.

Morgan, J.P., 1987. Melt migration beneath mid-ocean spreading centers. Geophys. Res. Lett. 14, 1238–1241. https://doi.org/10.1029/GL014i012p01238.

Morgan, J.P., Chen, Y.J., 1993. The genesis of oceanic crust: magma injection, hydrothermal circulation, and crustal flow. J. Geophys. Res., Solid Earth 98, 6283–6297. https://doi.org/10.1029/92JB02650.

Nadin, E.S., Saleeby, J., Wong, M., 2016. Thermal evolution of the Sierra Nevada batholith, California, and implications for strain localization. Geosphere 12, 377–399. https://doi.org/10.1130/GES01224.1.

Paterson, S.R., Ducea, M.N., 2015. Arc magmatic tempos: gathering the evidence. Elements 11, 91–98. https://doi.org/10.2113/gselements.11.2.91.

Ranalli, G., 1995. Rheology of the Earth. Springer Science & Business Media.

Reiners, P.W., Brandon, M.T., 2006. Using thermochronology to understand orogenic erosion. Annu. Rev. Earth Planet. Sci. 34, 419–466. https://doi.org/10.1146/annurev.earth.34.031405.125202.

Roland, E., Behn, M.D., Hirth, G., 2010. Thermal-mechanical behavior of oceanic transform faults: implications for the spatial distribution of seismicity. Geochem. Geophys. Geosyst. 11. https://doi.org/10.1029/2010GC003034.

Rothstein, D.A., Manning, C.E., 2003. Geothermal gradients in continental magmatic arcs: constraints from the eastern Peninsular Ranges batholith, Baja California, México. Spec. Pap., Geol. Soc. Am. 374, 337–354.

Saar, M.O., Manga, M., 2004. Depth dependence of permeability in the Oregon Cascades inferred from hydrogeologic, thermal, seismic, and magmatic modeling constraints. J. Geophys. Res. 109, 1–19. https://doi.org/10.1029/2003JB002855.

Schmeling, H., Marquart, G., 2014. A scaling law for approximating porous hydrothermal convection by an equivalent thermal conductivity: theory and application to the cooling oceanic lithosphere. Geophys. J. Int. 197, 645–664. https://doi.org/10.1093/gji/ggu022.

Sibson, R.H., 1982. Fault zone models, heat flow, and the depth distribution of earthquakes in the continental crust of the United States. Bull. Seismol. Soc. Am. 72 (1), 151–163.

Sousa, F.J., Saleeby, J., Farley, K.A., Unruh, J.R., Lloyd, M.K., 2017. The southern Sierra Nevada pediment, central California. Geosphere 13, 82–101. https://doi.org/10.1130/GES01369.1.

Stipp, M., Tullis, J., Behrens, H., 2006. Effect of water on the dislocation creep microstructure and flow stress of quartz and implications for the recrystallized grain size piezometer. J. Geophys. Res., Solid Earth 111. https://doi.org/10.1029/2005JB003852.

Stüwe, K., White, L., Brown, R., 1994. The influence of eroding topography on steady-state isotherms. Application to fission track analysis. Earth Planet. Sci. Lett. 124 (1–4), 63–74. https://doi.org/10.1016/0012-821X(94)00068-9.

Travis, B.J., Janecky, D.R., Rosenberg, N.D., 1991. Three-dimensional simulation of hydrothermal circulation at mid-ocean ridges. Geophys. Res. Lett. 18, 1441–1444. https://doi.org/10.1029/91GL01776.

Zhang, S.-H., Zhao, Y., Pei, J.-L., Zhang, Q.-Q., Miggins, D.P., Koppers, A.A.P., 2019. Paleogeotherms of a mid- to upper-crustal profile across the northern North China Block: implications for thermal structure of continental arcs. Tectonics, 1–41. https://doi.org/10.1029/2018TC005154.

Zuza, A.V., Carlson, C.W., 2018. What can strike-slip fault spacing tell us about the plate boundary of western North America? Terra Nova 30, 105–113. https://doi.org/10.1111/ter.12315.

Zuza, A.V., Yin, A., Lin, J., Sun, M., 2017. Spacing and strength of active continental strike-slip faults. Earth Planet. Sci. Lett. 457, 49–62. https://doi.org/10.1016/j.epsl.2016.09.041.